

Converging 3D Printing and Electrospinning: Effect of Poly(L-lactide)/Gelatin Based Short Nanofibers Aerogels on Tracheal Regeneration

Zhengchao Yuan, Yijiu Ren, Muhammad Shafiq,* Yujie Chen, Hai Tang, Baojie Li, Mohamed EL-Newehy, Hany EL-Hamshary, Yosry Morsi, Hui Zheng,* and Xiumei Mo*

Recently, various tissue engineering based strategies have been pursued for the regeneration of tracheal tissues. However, previously developed tracheal scaffolds do not accurately mimic the microstructure and mechanical behavior of the native trachea, which restrict their clinical translation. Here, tracheal scaffolds are fabricated by using 3D printing and short nanofibers (SF) dispersion of poly(L-lactide)/gelatin (0.5–1.5 wt%) to afford tracheal constructs. The results display that the scaffolds containing 1.0 wt % of SF exhibit low density, good water absorption capacity, reasonable degradation rate, and stable mechanical properties, which were comparable to the native trachea. Moreover, the designed scaffolds possess good biocompatibility and promote the growth and infiltration of chondrocytes *in vitro*. The biocompatibility of tracheal scaffolds is further assessed after subcutaneous implantation in mice for up to 4 and 8 weeks. Histological assessment of tracheal constructs explanted at week 4 shows that scaffolds can maintain their structural integrity and support the formation of neo-vessels. Furthermore, cell-scaffold constructs gradually form cartilage-like tissues, which mature with time. Collectively, these engineered tracheal scaffolds not only possess appropriate mechanical properties to afford a stabilized structure but also a biomimetic extracellular matrix-like structure to accomplish tissue regeneration, which may have broad implications for tracheal regeneration.

defects are usually caused by tumor, infection, and trauma, which can significantly affect the quality of life of an individual.^[2,3] When the defected region is more than 50% of the total tracheal length in adults or about 30% in pediatric patients, it is almost impossible to be regenerated by the conventional surgical methods, including an end-to-end anastomosis.^[4,5] This necessitates the implantation of tracheal substitutes for airway reconstruction.^[6,7] Tissue-engineered trachea scaffolds possessing sufficient mechanical strength and a proper luminal contour have gathered considerable attention of the research community for tracheal regeneration applications.^[8] An ideal tracheal implant should possess a tubular-shaped structure similar to that of the native trachea to maintain respiration,^[9] sufficient mechanical strength to avoid collapse, structural stability for an uninterrupted performance during implantation,^[10] a biomimetic extracellular matrix (ECM)-like structure to support cell adhesion and proliferation,^[7] and a desirable bioactivity to achieve tissue regeneration.^[11]

1. Introduction

The trachea is a hollow-structured organ that plays a vital role in respiration, phonation, and airway protection.^[1] The tracheal

Tissue engineering techniques provide promising alternatives for fabricating tracheal scaffolds.^[12] Decellularized tracheal matrix is a desirable substitute for tracheal regeneration due to its natural tubular structure, cartilage matrix components, and

Z. Yuan, M. Shafiq, Y. Chen, B. Li, X. Mo
 Shanghai Engineering Research Center of Nano-Biomaterials and Regenerative Medicine
 State Key Laboratory for Modification of Chemical Fibers and Polymer Materials
 College of Chemistry
 Chemical Engineering and Biotechnology
 Donghua University
 Shanghai 201620, P. R. China
 E-mail: dr.muhammadshafiq@ucp.edu.pk; xmm@dhu.edu.cn

Y. Ren, H. Tang, H. Zheng
 Department of Thoracic Surgery
 Shanghai Pulmonary Hospital
 Tongji University School of Medicine
 Shanghai 200433, P. R. China
 E-mail: 103341@tongji.edu.cn
 M. EL-Newehy, H. EL-Hamshary
 Department of Chemistry
 College of Science
 King Saud University
 P.O. Box 2455, Riyadh 11451, Saudi Arabia
 Y. Morsi
 Faculty of Engineering and Industrial Sciences
 Swinburne University of Technology
 Boroondara, VIC 3122, Australia

 The ORCID identification number(s) for the author(s) of this article can be found under <https://doi.org/10.1002/mabi.202100342>

DOI: 10.1002/mabi.202100342

biodegradability.^[13] However, the long-time needed for the tracheal decellularization may not be a feasible strategy, especially for the treatment of the neo-natal tracheal atresia or serious defects requiring an earlier tracheal replacement.^[14] Electrospun tracheal scaffolds have been demonstrated to be used for tracheal repair. However, the tracheal stenosis and collapse may hamper their clinical translation.^[14,15] Similarly, the poor mechanical properties and dense structure of hydrogels may limit their application for tracheal regeneration.^[16,17] Three-dimensional (3D) printing is a promising method for the precise fabrication of tracheal scaffolds that closely match the mechanical properties and architecture of patients' trachea,^[18] which has been widely exploited to fabricate tracheal implants.^[12,13] However, 3D-printed tracheal scaffolds experience significant drawbacks, including insufficient biocompatibility and less regenerative ability, which remains a great challenge due to the lack of structures and functions similar to the natural ECM.^[15,16]

Recently, electrospinning, a simple yet versatile technology, has gathered widespread attention of the research community due to the high porosity and large surface-area-to-volume ratio of the electrospun scaffolds.^[18,19] However, electrospun scaffolds are generally two-dimensional (2D) nanofibrous membranes comprising of densely-packed fibers layers with only superficial pores, which impede cell growth and cell infiltration.^[20,21] Thus, it is imperative to foster an innovative strategy to improve the microstructure of the electrospun scaffolds.

Herein, we conceived a biomimetic tracheal scaffold to mimic native ECM-like structure and mechanical behavior similar to the native trachea by simultaneously exploiting the advantages of 3D printing and electrospinning. The planar scaffolds were first fabricated by 3D printing, which were next amassed into a tubular shape. Polycaprolactone (PCL), which has good biocompatibility and biodegradability and has been widely explored for the fabrication of tissue engineering scaffolds, including artificial blood vessels and 3D-printed materials was chosen for the 3D printing of tubular scaffolds.^[22] Poly(L-lactide)/gelatin (PLLA/Gel) based scaffolds prepared by electrospinning have been shown to exhibit ECM-like structure as well as excellent biocompatibility and were therefore chosen as materials for the fabrication of the short nanofiber aerogels.^[23] The tracheal scaffolds were fabricated by combining tubular scaffolds and short nanofibers aerogels. We investigated their structural stability, mechanical properties, degradability, biocompatibility, and cell infiltration in vitro. Thereafter, we assessed the biocompatibility of scaffolds in vivo. The combinatorial approach encompassing 3D printing and short nanofibers self-assembly may have broad implications for tracheal regeneration applications.

2. Results

Tracheal scaffolds were fabricated by using tubular scaffolds and the different concentrations of short nanofibers aerogels. Both the short nanofiber aerogels and tracheal scaffolds were thoroughly characterized.

2.1. Preparation and Characterizations of Tracheal Scaffolds

The morphological analysis of the nanofibers was carried out by scanning electron microscopy (SEM), which displayed a

smooth and uniform morphology of nanofibers (Figure 1a). The PLLA/Gel nanofibers were next converted into short nanofibers by a high-speed homogenizer to realize their dispersion for incorporation into tracheal scaffolds (Figure 1b). Next, the 3D-printed planar scaffolds were fabricated into tubular scaffolds (Figure 1c). The number of the strands, layer thickness, diameter, and axial length of tubular scaffold were determined.

The tracheal scaffolds were fabricated by using 3D-printed tubular scaffolds and short nanofiber aerogels containing 0.5%, 1.0% and 1.5% of short nanofibers (SF0.5, SF1.0, and SF1.5 aerogels) and represented as TSF0.5, TSF1.0, and TSF1.5, respectively (Figure 1e–g). It was clearly observed from the SEM micrographs that the tracheal scaffolds had a porous architecture (Figure 1i–k). Aerogels were composed of a large number of short nanofibers exhibiting nonuniform and randomly distributed pores (Figure 1i–k insets). The cross-sections of TSF1.0 displayed the tubular scaffolds (TBS) and SF1.0 aerogels on both sides to afford composite construct (Figure 1h–i).

The tracheal scaffolds were designed to mimic the structure of the native trachea (NT) in a 3-month-old New Zealand white rabbit (weight 2.5–3.0 kg). To mimic the NT, the tracheal scaffolds should exhibit the morphology similar to the NT, including axial length, layer thickness, and diameter (Figure 2a,b). Table 1 showed the macroscopic characteristics of scaffolds and NT. The length of TBS, dry TSF1.0, wet TSF1.0, and NT did not appreciably differ from each other. The layer thickness of TBS, dry TSF1.0, wet TSF1.0, and native trachea was 0.79 ± 0.02 , 1.67 ± 0.13 , 1.25 ± 0.18 , and 0.83 ± 0.02 mm, respectively. The TSF1.0 displayed larger layer thickness than that of the NT, which is ascribed to the incorporation of the aerogels on both sides of the tracheal scaffolds. The addition of the short nanofibers aerogels also affected the diameter of tracheal scaffolds; which exhibited less diameter than that of the aerogel-free tubular scaffolds (inner diameter, TBS, 8.13 ± 0.06 mm; dry TSF1.0, 6.52 ± 0.24 mm; wet TSF1.0, 6.98 ± 0.30 mm; and NT, 5.97 ± 0.58 mm). The outer diameter of tracheal scaffolds was 9.63 ± 0.08 , 9.85 ± 0.21 , 9.48 ± 0.20 , and 7.37 ± 0.35 mm for TBS, dry TSF1.0, wet TSF1.0, and NT, respectively.

The porosity of SF0.5, SF1.0, SF1.5, and TSF1.0 was $97.4 \pm 0.1\%$, $93.2 \pm 0.6\%$, $91.0 \pm 0.8\%$, and $61.2 \pm 3.3\%$, respectively (Figure 3a). The density of SF0.5, SF1.0, SF1.5, and TSF1.0 was 12.3 ± 0.6 , 22.9 ± 0.6 , 27.7 ± 1.7 , and 179.0 ± 3.3 mg cm⁻³, respectively (Figure 3b). The TSF1.0 exhibited less porosity, whereas high density than that of the SF aerogels. The volume shrinkage rate of SF0.5, SF1.0, and SF1.5 was $28.7 \pm 0.4\%$, $26.7 \pm 0.4\%$, and $25.4 \pm 0.2\%$ in dry state, and $52.2 \pm 0.1\%$, $34.3 \pm 0.2\%$, and $29.4 \pm 0.2\%$ in wet state, respectively (Figure 3c). These results showed that the SF0.5 aerogels underwent severe volume shrinkage than that of the SF1.0 and SF1.5 aerogels in the wet state.

The water absorption of SF0.5, SF1.0, SF1.5, and TSF1.0 was $2847.9 \pm 289.9\%$, $2147.8 \pm 285.9\%$, $1633.1 \pm 141.5\%$, and $579.1 \pm 19.0\%$, respectively (Figure 3d). The aerogels achieved the maximum water absorption in less than 3 min, which showed their good water absorption capacity. On the other hand, the TSF1.0 took longer time for the water absorption (≈ 10 min), which is attributed to the hydrophobic nature of the PCL. Moreover, in the water absorption reversibility testing for up to 10 cycles, the SF1.0 and SF1.5 aerogels were compressed with a strain of 80% to remove most of the absorbed water. After the compressive force was

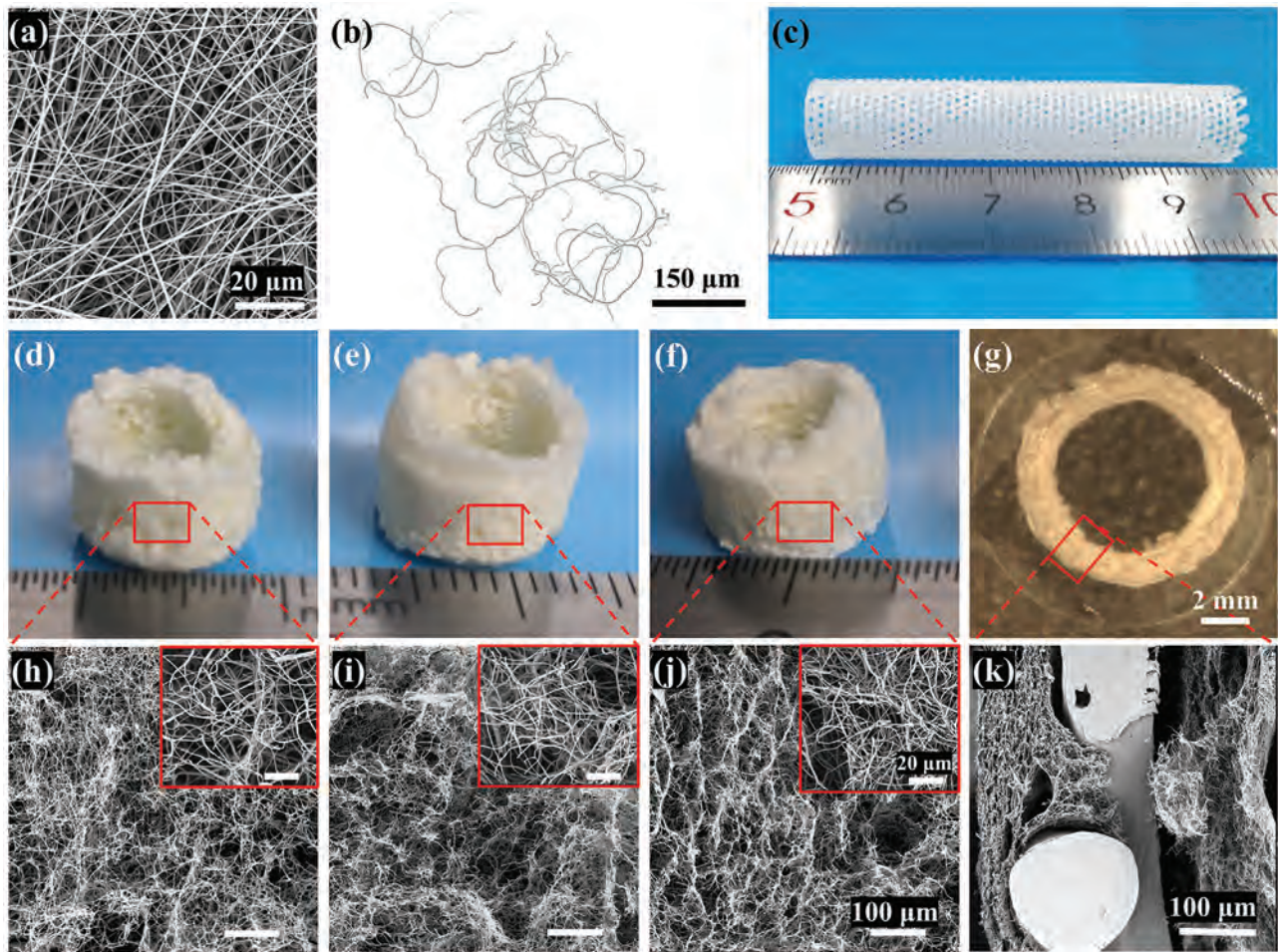


Figure 1. Morphological analysis of tracheal scaffolds. SEM image of PLLA/Gel electrospun nanofibers a). Optical microscope image of the homogenized short nanofibers b). Photograph of tubular scaffold (TBS) c). Representative photographs of TFS0.5 e), TFS1.0 f), TFS1.5 g), and TFS1.0 cross-section h). Representative SEM images of TFS0.5 i), TFS1.0 j), TFS1.5 k), and TFS1.0 cross-section l). Insets in show high magnification of areas in the corresponding images of tracheal scaffolds h–k). Scale bar, 2 mm g), 100 μm h–k), and 20 μm (insets h–j).

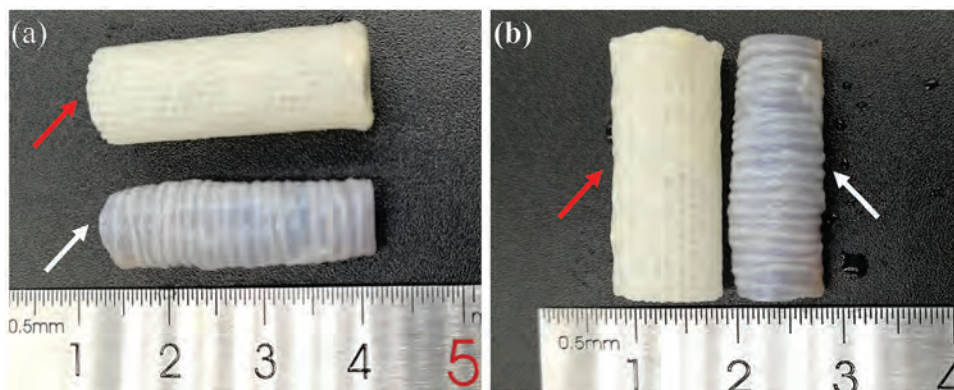


Figure 2. Macroscopic appearance of tracheal scaffold and native trachea. Representative photographs of length a) and diameter b) of wet TFS1.0 and native trachea. Red and white arrows indicate TFS1.0 and native trachea, respectively.

Table 1. Morphological characteristics of native trachea and tracheal scaffolds.

| Index ^a (n = 5) | NT | TBS | Dry TSF1.0 | Wet TSF1.0 |
|----------------------------|-----------|-----------|------------|------------|
| Axial length [cm] | 3.50±0.12 | 3.55±0.03 | 3.55±0.03 | 3.55±0.03 |
| Layer thickness [mm] | 0.83±0.02 | 0.79±0.02 | 1.67±0.13 | 1.25±0.18 |
| Inner diameter [mm] | 5.97±0.58 | 8.13±0.06 | 6.52±0.24 | 6.98±0.30 |
| Outer diameter [mm] | 7.37±0.35 | 9.63±0.08 | 9.85±0.21 | 9.48±0.20 |

relieved, the scaffolds absorbed water and recovered to their original shapes with no loss for the water absorption capacity (Figure 3e).

2.2. Evaluation of Mechanical Properties

Mechanical properties, such as ultimate tensile stress (UTS), Young's modulus (E), and elongation at break (E_b) of TBS and NT were evaluated and shown in Figure 4. While both groups followed the Hooke's law during the initial stage of stretching, the TBS underwent deformation beyond the yield point as the stress was increased due to the elongation of the PCL (Figure 4b). The E_b of TBS and NT was $226.3 \pm 11.0\%$ and $142.1 \pm 14.4\%$, respectively (Figure 4c). Meanwhile, the UTS and E of NT were lower than that of the tubular scaffolds (UTS, NT, 0.52 ± 0.06 MPa and TBS, 3.79 ± 0.06 MPa; E , NT, 0.10 ± 0.01 MPa and TBS, 42.03 ± 1.44 MPa) (Figure 4d,e).

TBS, dry TSF1.0, wet TSF1.0, and NT also underwent radial compression testing for up to 50 loading-unloading fatigue cycles ($\epsilon = 50\%$) (Figure 5a). No significant decrease in the stress was observed for the scaffolds after 50 cyclic compressions, which displayed their excellent performance during compression testing (Figure 5b–e). In the first cycle of the compression test, the com-

pressive stress at 50% deformation was found to be 39.83 ± 1.59 , 32.49 ± 5.05 , 26.96 ± 0.84 , and 18.70 ± 3.36 MPa for TBS, dry TSF1.0, wet TSF1.0, and NT, respectively (Figure 5f), which indicated that the compressive stress of scaffolds was significantly higher than that of the NT. Similarly, E of TBS, dry TSF1.0, wet TSF1.0, and NT was 70.72 ± 14.29 , 46.19 ± 11.17 , 20.86 ± 3.13 , and 19.30 ± 4.96 MPa, respectively (Figure 5g); there was no significant difference in the E between wet TSF1.0 and NT. Moreover, tracheal scaffolds and NT did not differ in term of the elastic recovery, which was statistically insignificant among different groups (Figure 5h). The results of elastic recovery rate indicated that TBS, dry TSF1.0, wet TSF1.0, and NT could bear a compressive strain as higher as 50% and recover to their original shapes after the stress is released. Wet TSF1.0 and NT better preserved the maximum stress value with less stress loss after 50 cycles of compression at 50% strain than that of the TBS, dry TSF1.0 (Figure 5i,j). Furthermore, the elastic performance of wet TSF1.0 was analogous to that of NT in the loading–unloading fatigue cycles.

2.3. Degradation of Scaffolds In Vitro

The evaluation of the degradation of the scaffolds is very important to assess the structural stability and morphology. As depicted in Figure 6a, all samples tended to degrade over time; the remaining mass after degradation was found to be $96.92 \pm 1.29\%$, $95.71 \pm 2.13\%$, and $83.72 \pm 3.83\%$ in the TBS, TSF1.0, and SF1.0 aerogel groups, respectively, after 12 weeks in vitro. SF1.0 aerogels displayed significantly higher weight loss than that of the TBS and TSF1.0 beyond the week 2, which may be ascribed to the degradation of the gelatin in the SF1.0 aerogel. Furthermore, the aerogel of TSF1.0 did not fall off until week 12, which indicated their good structural stability (Figure 6b,c). The degradation of the scaffolds was further ascertained by morphological observations by using scanning electron microscopy (SEM) as shown

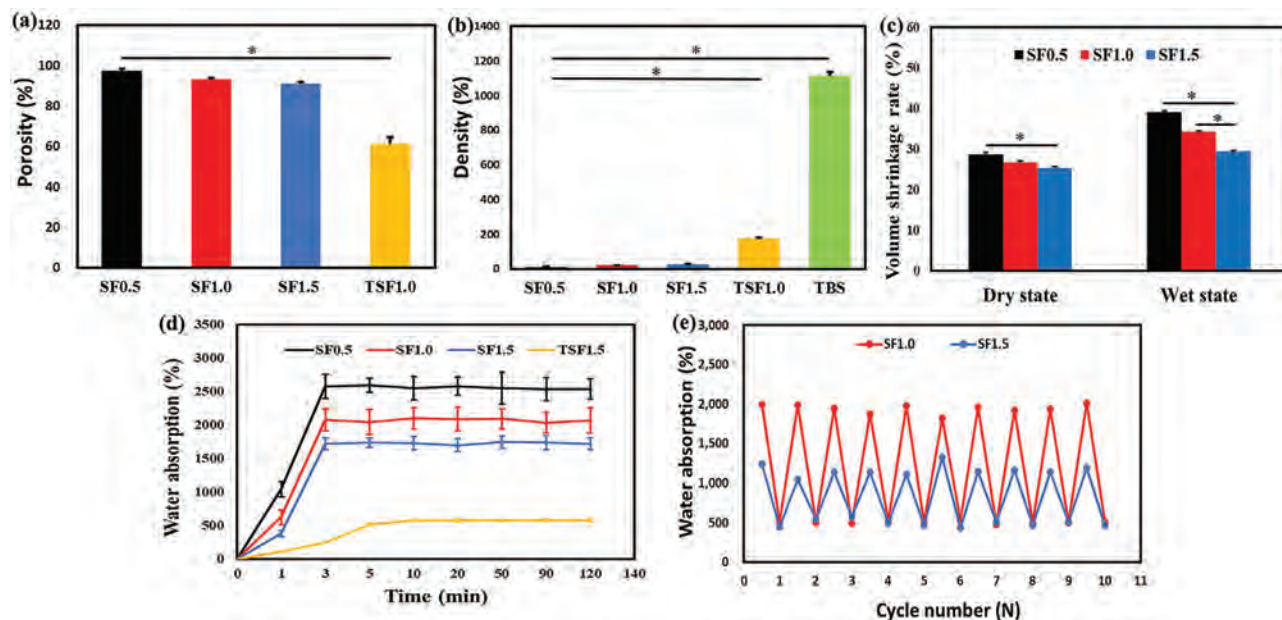


Figure 3. Characterization of aerogels and tracheal scaffolds. The porosity a), density b), volume shrinkage rate c), water absorption d), and water absorption reversibility e) of samples ($n = 5$). $*p = 0.05$.

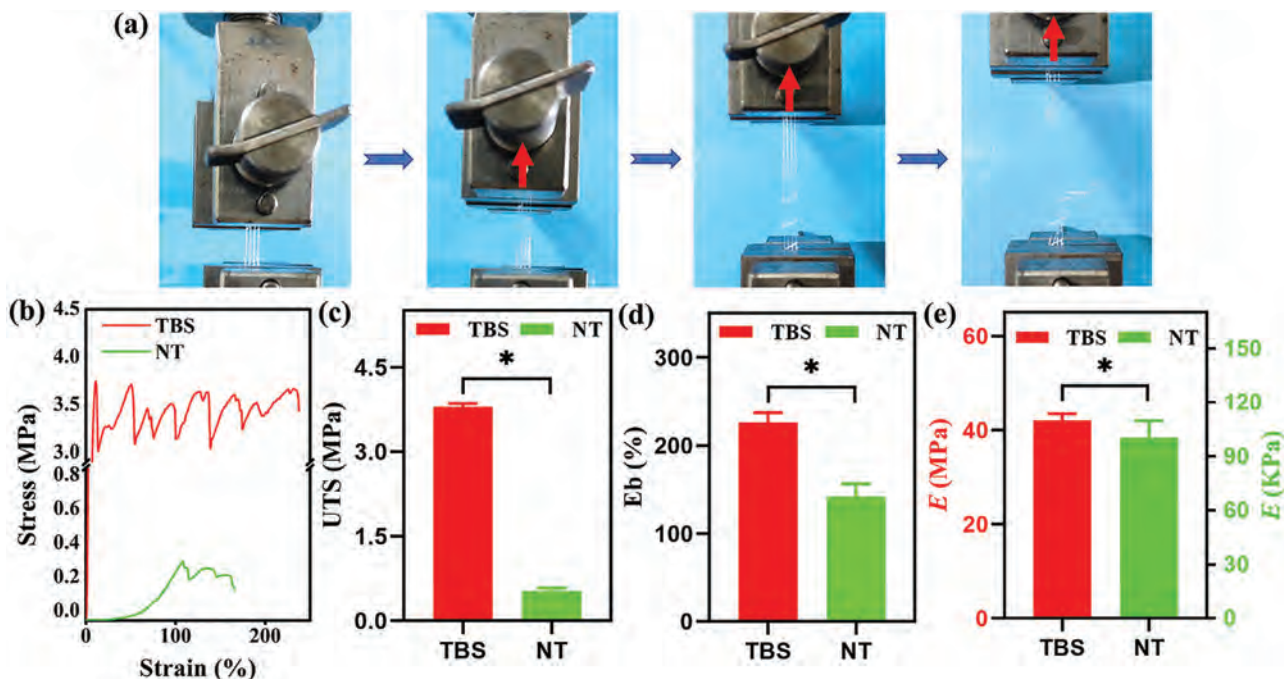


Figure 4. Longitudinal tensile testing of tubular scaffold and NT. Photographs of the tubular scaffold (TBS) during elongation a), tensile stress–strain curves of TBS and NT b), ultimate tensile stress (UTS) c), Young's modulus (E) d), elongation at break (Eb) e) of TBS and native trachea ($n = 5$). * $p = 0.05$.

in Figure 6d. The morphology of TBS did not substantially alter during the investigation period. Similarly, TSF1.0 exhibited intact structures of the SF aerogel in cross-sectional view, which did not change. By contrast, the morphology of the TSF1.0 surface aerogel changed at 4, 6, 8, and 12 weeks from well-defined fibrous structure to the slightly swollen state of the fibers due to the degradation of the aerogel on the nanofibers. The degradation results displayed that the TSF1.0 could maintain their structural stability as long as 12 weeks.

2.4. Biocompatibility of Scaffolds In Vitro

The hemolysis test was carried out to investigate the hemocompatibility of tracheal scaffolds in vitro. The hemolysis ratio of TBS, TSF0.5, TSF1.0, and TSF1.5 was found to be $0.84 \pm 0.5\%$, $0.93 \pm 0.6\%$, $0.86 \pm 0.2\%$, and $1.52 \pm 0.3\%$, respectively (Figure 7a). The hemolysis ratio of scaffolds was less than 2%, which demonstrated their good hemocompatibility.^[24] To further discern the biocompatibility of the scaffolds, the cell seeding efficiency was determined, which was found to be $82.5 \pm 1.7\%$, $92.2 \pm 3.4\%$, and $96.1 \pm 1.9\%$ for TSF0.5, TSF1.0, and TSF1.5 scaffolds, respectively (Figure 7b). The tracheal scaffolds showed higher numbers of cells than that of the SF aerogels, which may be ascribed to their 3D porous structure conducive for cell proliferation and adhesion.

Moreover, the cell proliferation of scaffolds was measured by cell counting kit-8 (CCK-8) assay, which showed that the proliferation of chondrocytes was increased with the time, further indicating about the biocompatibility of scaffolds (Figure 7c). However, no significant difference in the cell proliferation was observed

among different groups of tracheal scaffolds. The live/dead staining assay also indicated the higher survival of cells on the tracheal scaffolds in vitro for up to 7 days (Figure 7d). Cell proliferation and cell adhesion of scaffolds was further observed by SEM (Figure 7e). Chondrocytes attached well and spread nicely on the tracheal scaffolds. The nanofibrous surfaces of TSF1.0 and TSF1.5 were completely covered by the chondrocytes after a culture for up to 7 days, which were consistent with the live and dead staining assay results. Taken together, these results indicate good biocompatibility of tracheal scaffolds.

2.5. Evaluation of Cell Infiltration into Scaffolds In Vitro

All of the tracheal scaffolds maintained their tubular shapes after being seeded with chondrocytes in vitro for up to day 7 (Figure 8a–c). However, the longitudinal sections of TSF0.5 exhibited structural instability demonstrating less adhesion between the aerogels and scaffold, which may be ascribed to the volume shrinkage of SF0.5 aerogel in the wet state (Figure 3c). The thickness of the slices during the hematoxylin and eosin (H&E) staining also confirmed the volume shrinkage of short fiber aerogel. To investigate cell infiltration into tracheal scaffolds, H&E staining at day 7 was performed, which established that the chondrocytes not only accumulated on the surface of scaffolds but also infiltrated into the scaffolds (Figure 8d–f). Moreover, chondrocytes penetrated deeply into the TSF0.5 and TSF1.0 scaffolds than that of the TSF1.5 group (Figure 8g–i). The scarcity of cells in the cross-section of TSF1.5 may be due to the difficulty for cells to infiltrate in the SF1.5 aerogels. Overall, the TSF1.0 scaffolds proved

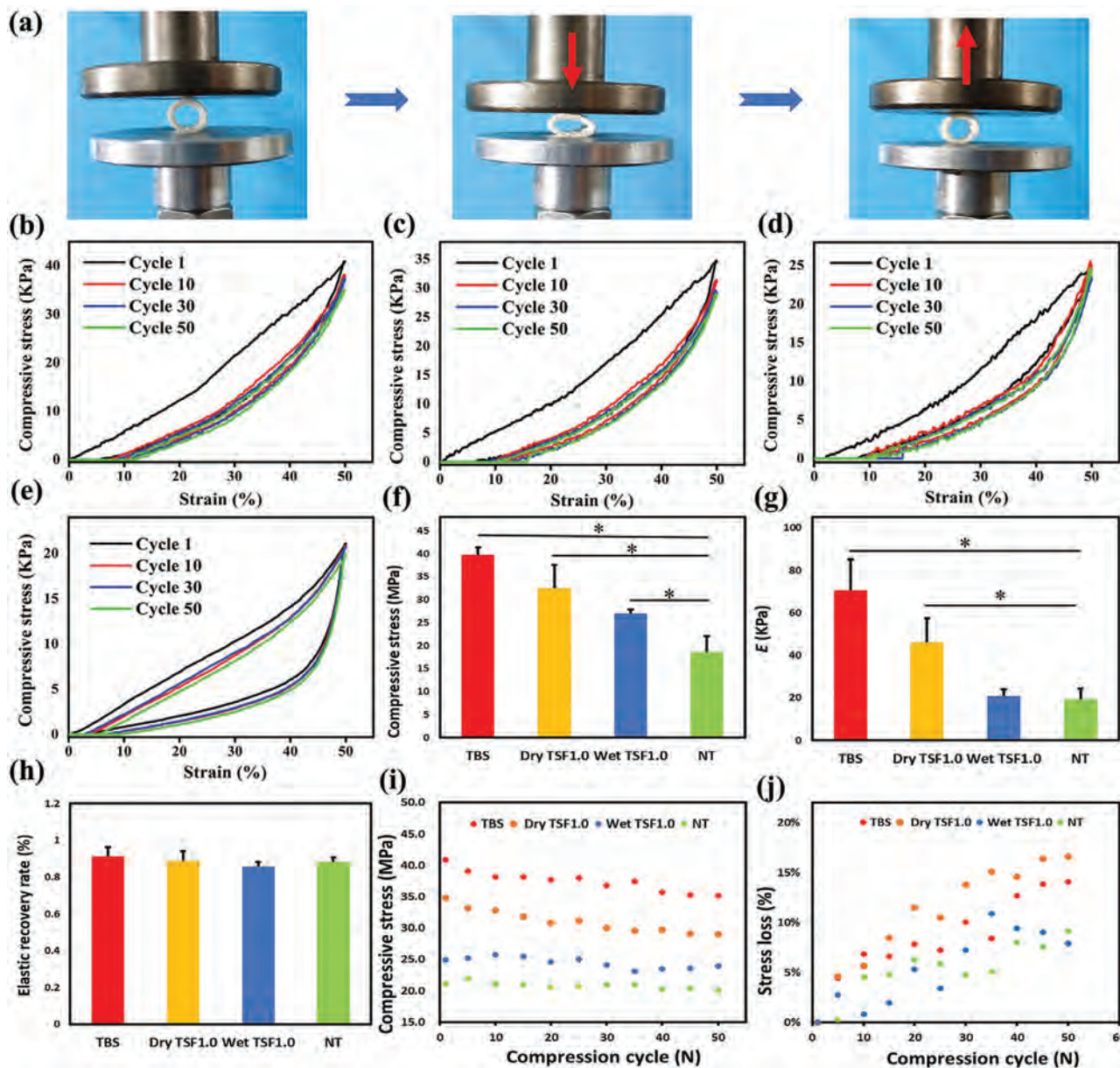


Figure 5. Radial compression testing of tracheal scaffolds and native trachea. a) Photographs of the dry TSF1.0 under a compressing and releasing cycle. Compressive stress–strain curves of the TBS b), dry TSF1.0 c), wet TSF1.0 d), and native trachea e) under different cycles in the compressive fatigue test ($\epsilon = 50\%$) ($n = 5$). The maximum compressive stress f), E g), and elastic recovery rate h) of the scaffolds in the first compressing test ($n = 5$). The history of i) maximum stress and j) stress loss as a function of compressive test cycles (50 cycles). * $p = 0.05$.

to be better candidates in terms of the cell infiltration and structural stability.

2.6. Preliminary Evaluation of Biocompatibility of Scaffolds In Vivo

The biocompatibility of TSF1.0 scaffolds was further assessed after subcutaneous implantation into mice for up to 4 weeks. TSF1.0 scaffolds maintained their gross appearance and supported cell infiltration into the scaffolds, establishing good structural stability and biocompatibility in vivo (Figure 9a–c). Masson's

trichrome staining revealed the formation of the collagenous tissues in the outer layers of the scaffolds (Figure 9e,h). The CD31 staining of scaffolds showed the regeneration of blood vessels (Figure 9f,i).

2.7. Evaluation of Cartilage Formation In Vivo

To discern the regenerative potential of chondrocytes-seeded tracheal patches in vivo, TSF0.5, TSF1.0, and TSF1.5 patches were implanted subcutaneously in mice for up to 4 and 8 weeks. The gross view of implants revealed the regeneration of a smooth

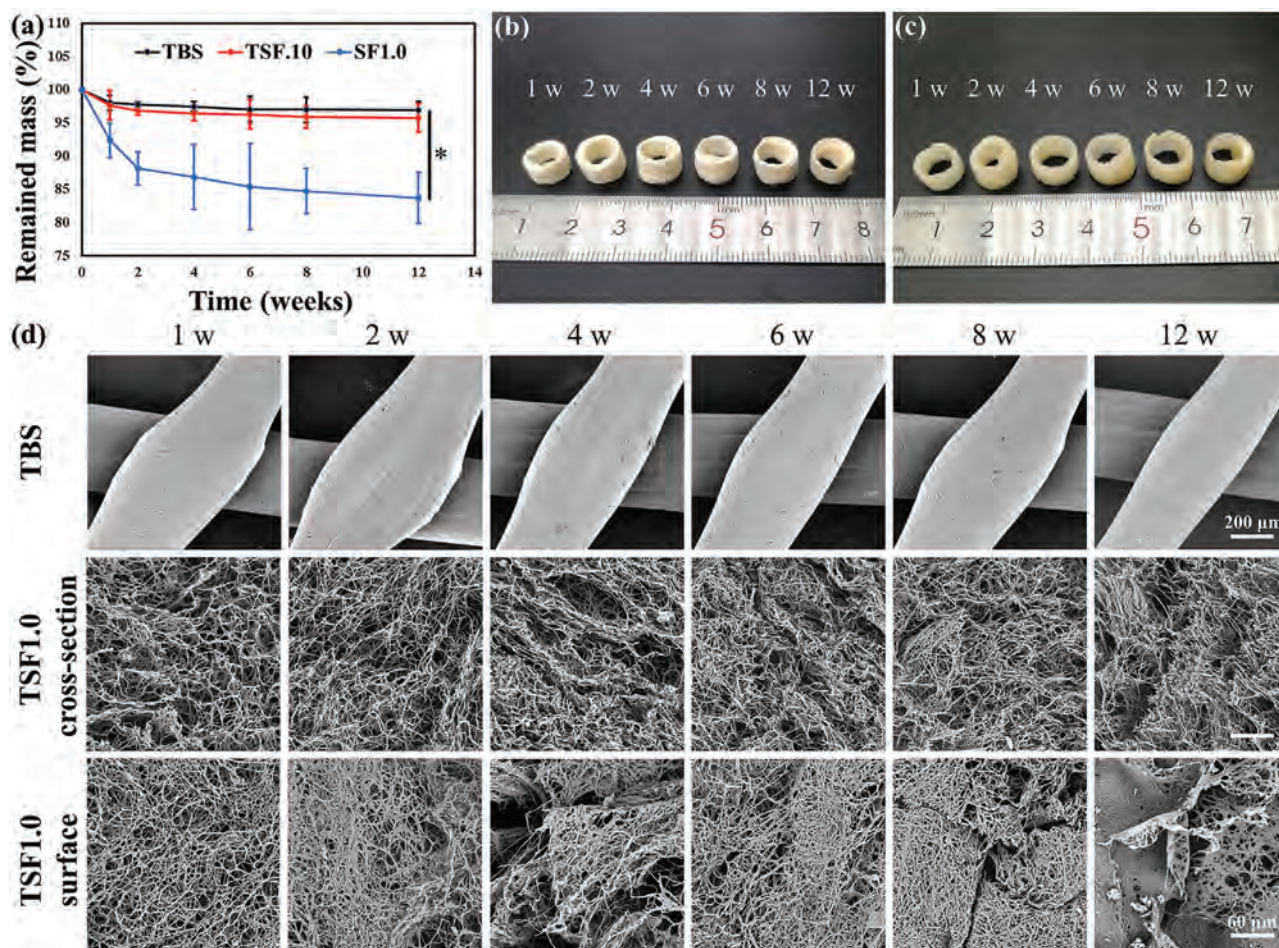


Figure 6. Degradation of scaffolds in vitro. Remaining mass of scaffolds after degradation for up to 12 weeks in vitro a). Macroscopic appearance of dry TSF1.0 b) and wet TSF1.0 c) after degradation for up to different time points. d) SEM images of scaffolds after degradation. $*p = 0.05$. Scale bar, 200 μm (TBS) and 60 μm (TSF1.0).

surface of the cartilage-like tissues (**Figure 10a**). H&E staining showed that the chondrocytes progressively infiltrated into scaffolds, which became further evident 8 weeks after implantation (**Figure 10b**). Meanwhile, the fibers gradually degraded and replaced by the growing cells. The explanted scaffolds also showed the deposition of cartilaginous ECM as shown by the Safranin-O (**Figure 10c**) and collagen type II (**Figure 10d**) staining 4 and 8 weeks after implantation. Collectively, these results indicate that these scaffolds may have broad implications for tracheal regeneration applications.

3. Discussion

Tracheal degeneration may lead to several complications affecting the life-style of an individual, which necessitates the design of tracheal scaffolds for tissue reconstruction. While tissue-engineered tracheal scaffolds possess great potential for the replacement of defected tracheal tissues, fabricating a suitable tracheal candidate mimicking the NT structurally and functionally still faces numerous challenges.^[3,24] Fabrication techniques, such as electrospinning and 3D printing can be exploited to fabricate tracheal scaffolds.^[25] However, tracheal scaffolds fabricated

from each of these techniques face several limitations; electrospun nanofibers exhibit compact structure, which may impede the diffusion of nutrients and oxygen as well as the infiltration of cellular components and tissues into scaffolds.^[26] While different types of postmodification approaches have been put forward to improve the porosity and pore size of electrospun scaffolds, they may compromise the physical properties of scaffolds.^[27] In this study, we prepared hybrid tracheal scaffolds assembling 3D printed planar scaffolds and short nanofibers aerogel; the aerogel could closely mimic the tracheal microenvironment as well as confer biocompatibility to the tracheal scaffolds.^[23] The tubular scaffold possessed similar mechanical behavior as that of the NT. Aerogel, as a main component of the tracheal scaffolds, plays a vital role imparting the biocompatibility to the scaffolds.

The uniform nanofibers were prepared by electrospinning and short nanofiber dispersions were obtained by homogenization (**Figure 11a**). To determine the appropriate pore size of aerogel conducive for cell growth and optimize the structural stability of tracheal scaffolds, we fabricated aerogels containing three different concentrations of short nanofiber dispersions (0.5–1.5 wt%). The pore diameter and volume shrinkage of tracheal scaffolds decreased with an increase in the concentration of the

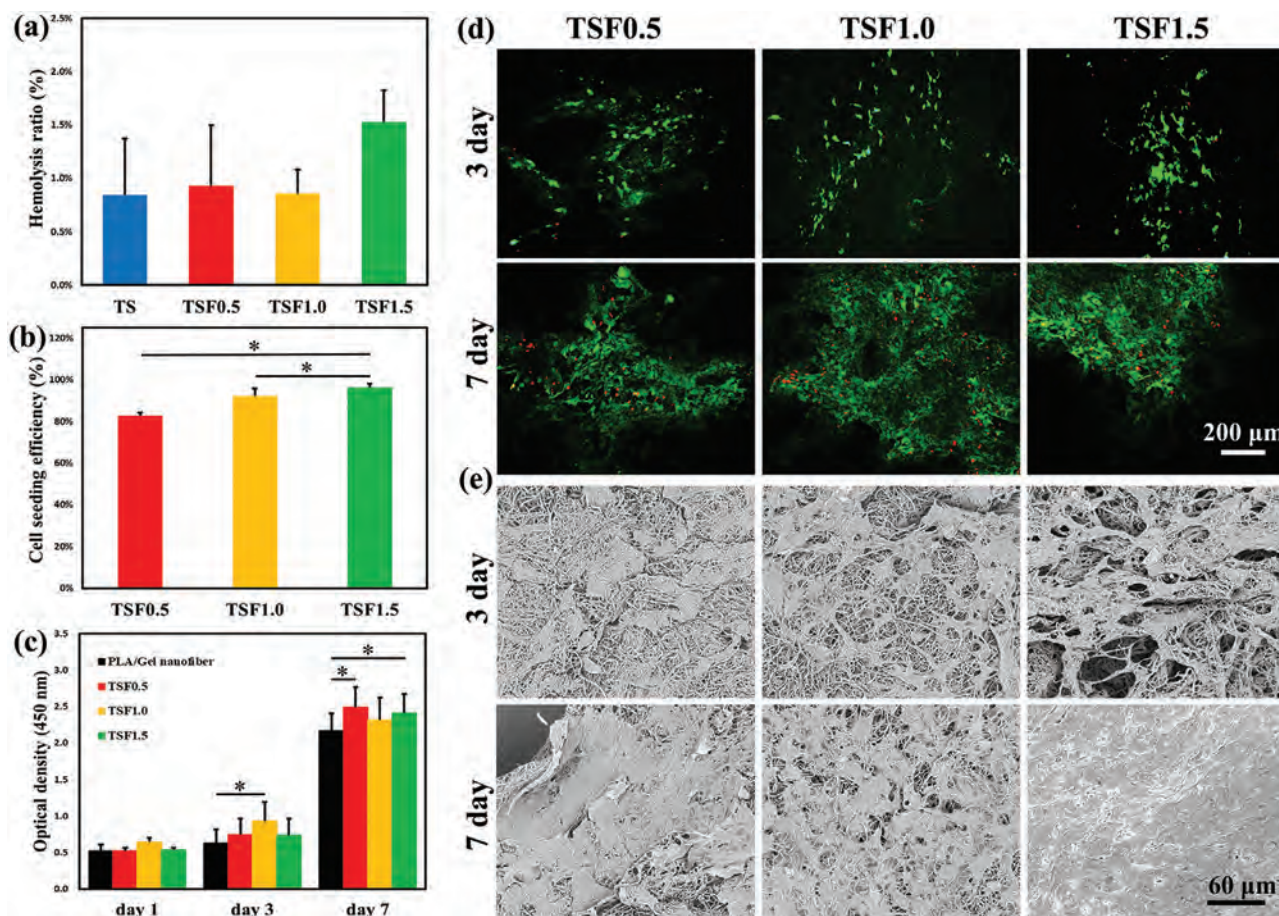


Figure 7. Evaluation of biocompatibility of scaffolds in vitro. Hemolysis ratio a) and cell seeding efficiency b). Proliferation of chondrocytes on scaffolds for up to 1, 3, and 7 days c). Live/dead staining assay d) and SEM images e) of chondrocytes cultured on scaffolds for up to 3 and 7 days (live and dead cells were stained in green and red, respectively). * $p = 0.05$. Scale bar, 200 μm d) and 60 μm e).

short nanofibers. The short nanofibers aerogels of tracheal scaffolds exhibited fibrous structure, displayed high porosity, and low density, mimicking the architecture of the native ECM.^[28] Furthermore, the aerogel of tracheal scaffolds possessed interconnected and hierarchically-structured pores with sizes ranging from sub-micrometers to ≈ 200 nm (Figure 1i–k), which may have significant impact on the nutrients diffusion, cellular proliferation and migration, and tissue formation.^[29,25] In addition, the aerogels exhibited excellent water absorption even after repeated cycles (Figure 3d,e), which may be very beneficial for the hydrophilicity of scaffolds as well as for cell adhesion and growth.^[30,26]

Different types of techniques can be employed to fabricate tracheal scaffolds, such as 3D printing, electrospinning, and salt-leaching.^[12,31] 3D printing can help design customized scaffolds, while electrospinning can help realize the nano- and microfibers with tunable diameter and porosity.^[32,33] Herein, we simultaneously leveraged 3D printing and electrospinning to fabricate planar scaffolds and short nanofibers aerogels, respectively, which were subsequently assembled into tubular tracheal scaffolds. It is envisioned that the 3D printed planar scaffolds may impart structural integrity to the tracheal scaffolds, while the SF aerogels can enhance cellularization as well as tissue regeneration

into scaffolds. It is noteworthy to mention here that, while, the tubular scaffolds can be directly fabricated by 3D printing, which is a more convenient method, it however, may require sophisticated experimental infrastructure.^[34,35] Consequently, we have fabricated planar scaffolds and then performed thermoforming to afford tubular shapes. Parallely, the scaffolds could be modified with the PCL/Gel dispersion by thermally-induced phase separation. Our rationale of employing electrospinning was to afford short nanofibers, which can then be homogeneously mixed with the scaffolds. Since electrospun nanofibers exhibit ECM-like morphology, we foresee that the modification of scaffolds with the short nanofibers may help recapitulate some of the features of the ECM.^[36,37]

Our results displayed that the length of the TSF1.0 was similar to that of the NT, while the layer thickness and diameter of TSF1.0 were higher than that of NT due to the incorporation of aerogels. Previous studies reported that the layer thickness and diameter of tracheal implants around 0.8–1.5 and 6.5–10.0 mm, respectively were acceptable for in vivo implantation of tracheal scaffolds.^[3,38,31] Therefore, the layer thickness (1.25 mm), inner luminal diameter (6.98 mm), and outer diameter (9.48 mm) of TSF1.0 did not exceed the acceptable range of tracheal scaffolds (Table 1).^[38,39]

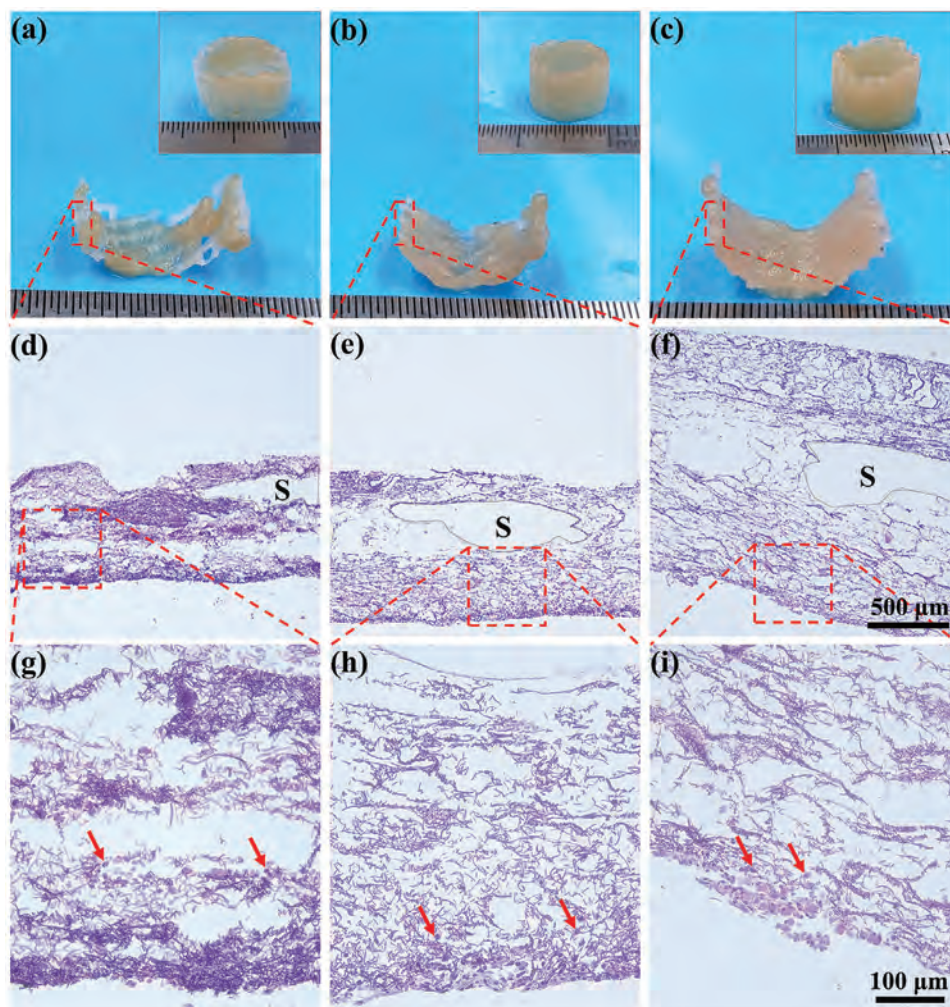


Figure 8. Gross view and histological analysis of cell-seeded tracheal scaffolds in vitro. Macroscopic appearance of TSF0.5 a), TSF1.0 b), and TSF1.5 c). H&E staining of TSF0.5 d,g), TSF1.0 e,h), and TSF1.5 f,i) at day 7. Red arrows indicate chondrocytes. (S = solid line of tubular scaffold). Scale bar, 500 μm d–f) and 100 μm g–i).

Native trachea is subjected to external pressures from the surrounding tissues, so the mechanical properties of the tracheal scaffolds are a critical indicator of whether they can be used for tracheal reconstruction in vivo.^[19] Accordingly, tracheal scaffolds should withstand tensile stresses resulting from the tissue movement.^[27,28] To ascertain the potential of tracheal scaffolds for in vivo implantation, mechanical properties of tracheal scaffolds as well as NT were measured. Tracheal scaffolds displayed E and UTS higher than that of the NT. To avoid the luminal collapse due to a higher external pressure than that of the internal luminal pressure, the radial compression tests were also carried out.^[27,39] Tracheal scaffolds as well as NT preserved the maximum stress value with minimum stress loss after 50 cycles of compression at 50% strain (Figure 5i,j). Furthermore, Young's moduli and elastic recovery rate of TSF1.0 closely matched to those of the NT in the wet state, indicating that the composite scaffold could be comparable to the radial load-bearing capacity of NT (Figure 5g,h).^[40]

Some problems, such as tracheal softening, collapse, and restenosis during the tracheal regeneration require to be pre-

vented and a reasonable degradation rate of scaffolds comparable to the tissue regeneration is required for an effective tissue repair.^[17] Although SF1.0 aerogels showed degradation as earlier as 2 weeks, PCL accounted for the remaining mass of TSF1.0 which may require a prolonged degradation period until the complete regeneration of the neo-trachea (Figure 6a).^[34,36] Furthermore, the morphology of aerogels in the tracheal cross-section of TSF1.0 did not substantially alter even after 12 week in vitro, which may afford a stable microenvironment and mechanical support as well as cell growth for tracheal regeneration (Figures 6d and 7c).^[20]

Biocompatibility is one of the fundamental requirements for the application of biomaterials in tissue engineering.^[41] Tracheal scaffolds displayed a low hemolysis ratio, which may have implications for constructing blood-contacting devices (Figure 7a). Besides, TSF1.0 and TSF1.5 scaffolds exhibited better cell seeding efficiency than that of the TSF0.5 scaffolds, which may be attributed to the more content of collagen in these scaffolds as well as an appropriate pore size of aerogels in the wet state.^[42]

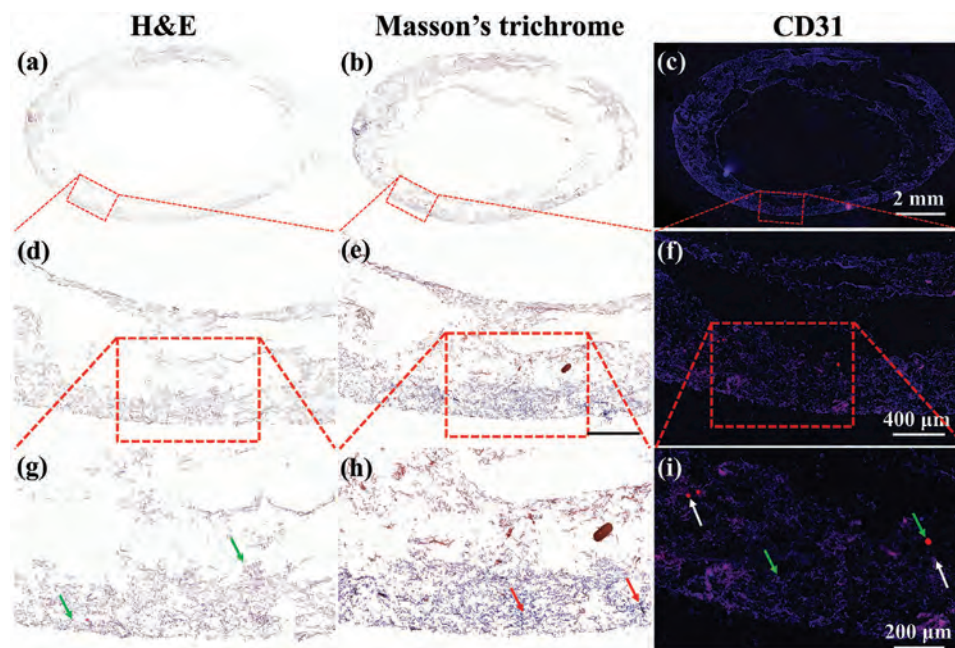


Figure 9. Histological and immunohistochemical analysis of TSF1.0 scaffolds after subcutaneous implantation in mice for up to 4 weeks. H&E staining (a,d,g), Masson's trichrome staining (arrows indicating toward the area with the collagen deposition) b,e,h), and immunofluorescence staining for CD31 (CD31⁺ cells and nuclei were stained in red and blue color, respectively) c,f,i). Scale bar, 2 mm a–c), 400 μm d–f), and 200 μm g–i).

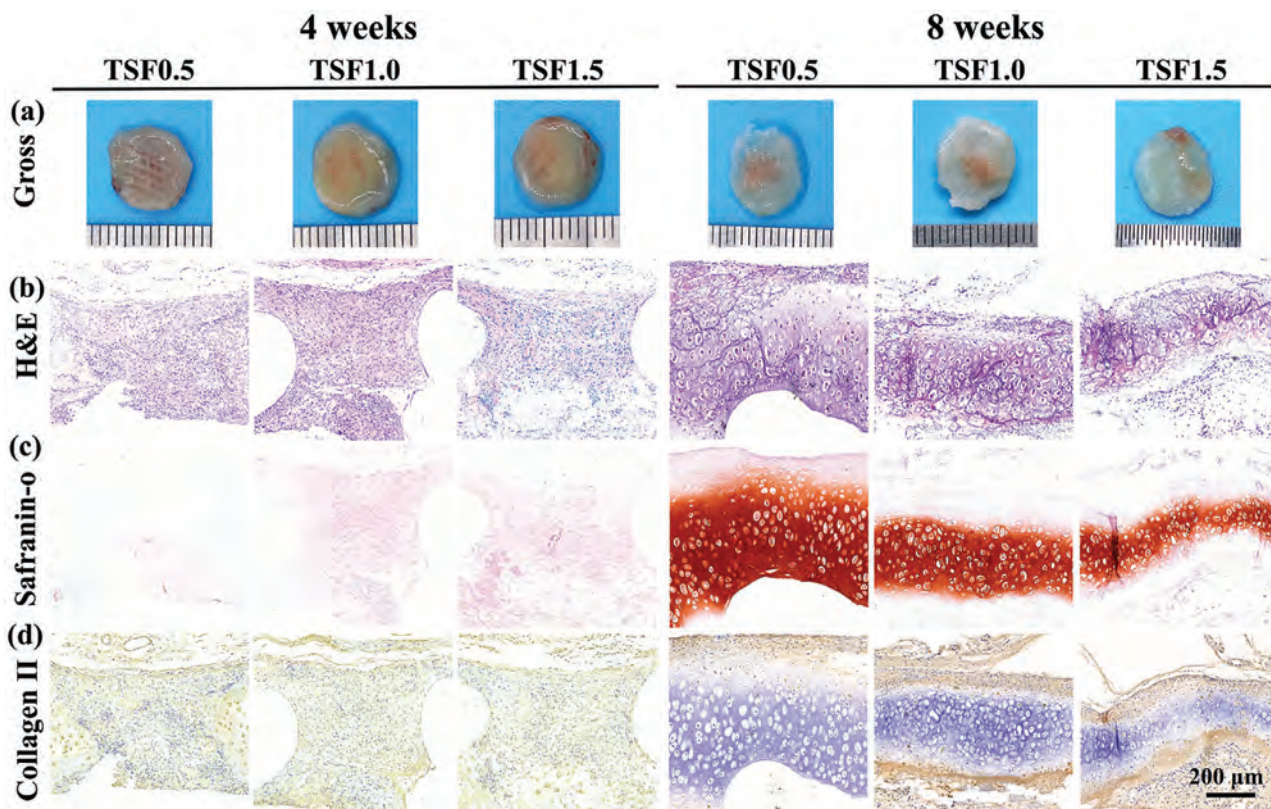


Figure 10. Gross view and histological analysis of chondrocyte-seeded tracheal patches after subcutaneous implantation in nude mice for up to 4 and 8 weeks. Gross view of TSF0.5 patch, TSF1.0 patch, and TSF1.5 patch 4 and 8 weeks after implantation a). Histological analysis of scaffolds by H&E b), Safranin-O c), and collagen type II d). Scale bar, 200 μm b–d).

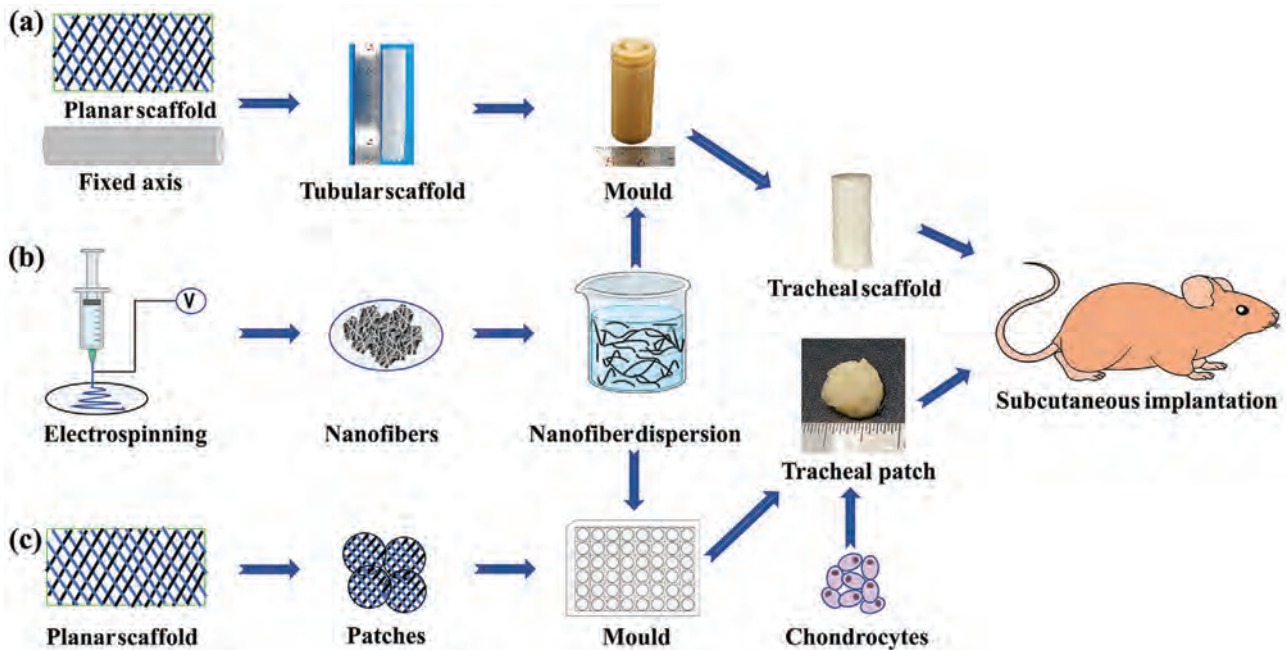


Figure 11. Schematic illustration of the fabrication of tracheal scaffolds a), the fabrication of short nanofibers b), and the fabrication of tracheal patches c).

Evaluation of cytocompatibility further demonstrated that the tracheal scaffolds could promote the adhesion, proliferation, and infiltration of chondrocytes (Figure 7c–e). Moreover, from the H&E staining results, cell infiltration was observed in all of the tracheal scaffolds (Figure 8g–i); the depth of the cell infiltration was higher in TSF0.5 and TSF1.0 scaffolds than that of the TSF1.5, which may be ascribed to their porous structure.^[43]

Vascularization and chondrification are also good indicators for the regeneration of the tracheal defects.^[13] Thus, we further investigated structural stability, biocompatibility, and vascularization of TSF1.0 scaffolds *in vivo*, which confirmed that they could maintain their initial appearance, promote cell growth, improve collagen deposition, and support new blood vessel formation, which may have implications for the remodeling of tracheal scaffolds upon implantation (Figure 9). As for the chondrification *in vivo*, we adopted a previously established strategy by implanting patch-type tracheal scaffolds to evaluate cartilage regeneration.^[44] The results indicated that the patch scaffolds could form cartilage-like tissue with an increase in the culture time to achieve chondrification *in vivo* (Figure 10). These results demonstrate that the fabrication of tracheal scaffolds with stable mechanical properties and adequate biocompatibility could be a promising approach for tracheal regeneration.

Taken together, our approach of leveraging 3D printing, electrospinning, and thermoforming represents an innovative paradigm which may have broad implications for tracheal regeneration by providing mechanical properties comparable to the native aorta and a biomimetic ECM-like structure. Whereas encouraging results are obtained in this project, several limitations still need to be addressed, such as inducing regeneration, cartilage growth, vascularization, and epithelialization.^[13] First, the epithelialization of tracheal implants is a crucial indicator to achieve

the early functioning of the neo-trachea, which warrants further evaluation of the biocompatibility of tracheal scaffolds.^[32,33] Second, growth factors can be installed into tracheal scaffolds and the microarchitecture can be improved to promote cellular activity and cartilage regeneration.^[45,42] Third, we evaluated the biocompatibility of tracheal scaffolds in a subcutaneous implantation model, which however, does not accurately mimic the tracheal microenvironment. Therefore, further studies should seek to investigate the optimization of the structure, tissue regeneration and functional restoration after implantation of tracheal scaffolds.

4. Conclusions

In summary, this study reports tracheal scaffold based on 3D printed planar scaffolds and electrospun short nanofibers aerogels. The 3D-printed planar scaffolds confer mechanical characteristics to maintain the structural stability of tracheal scaffolds and short nanofibers aerogel mimic the native ECM-like structure of the trachea to realize the tracheal regeneration. Tracheal scaffolds containing SF aerogels (1.0 wt% of nanofibers) exhibited mechanical properties similar to that of the native trachea as well as a reasonable degradation rate to afford a stable microenvironment for tissue regeneration. Biocompatibility results displayed that tracheal scaffold possessed a suitable cell seeding efficiency, good hemocompatibility, as well as potential to promote cell growth and neo-tissue formation. Evaluation of cartilage formation and biocompatibility *in vivo* further indicated that tracheal scaffolds could improve collagen accumulation, support new blood vessel formation, and accomplish the cartilage regeneration. Therefore, the strategy of engineering tracheal scaffolds by assembling different fabrication techniques and incorporating

short nanofibers aerogels may have broad implications for tissue engineering applications.

5. Experimental Section

Materials: Gelatin (Gel, 48722-500G-F) was purchased from MP Biomedicals, LLC (Shanghai, China). Poly (L-lactic acid) (PLLA, $M_n = 300$ kDa) was provided by Medprin Regenerative Medical Technologies Co., Ltd (Shanghai, China). Polycaprolactone (PCL, $M_n = 80$ kDa) was obtained from Jinan Daigang Biomaterial Co., Ltd (Jinan, China). Glutaraldehyde and *tert*-butanol were purchased from Sinopharm Chemical Reagent Co., Ltd (Shanghai, China). 1,1,1,3,3,3-hexafluoro-2-propanol (HFIP) was purchased from Shanghai Darui Fine Chemical Co., Ltd (Shanghai, China). Chondrocytes were isolated from the auricular cartilage of New Zealand white rabbits. All other chemicals were of analytical grade and used without any further purification.

Fabrication of 3D Printed Tracheal Scaffolds—Preparation of Short Nanofiber Dispersions: To prepare SF dispersions, about 2 g of PLLA and Gel (2:8 w/w) were dissolved in 20 mL of HFIP until the clear solution was obtained (Figure 11a). Following electrospinning conditions were used to afford nanofibrous membranes: voltage, 12 kV, flow rate, 2.5 mL h⁻¹, and distance between the spinneret and collector, 10–15 cm. Membranes were dried under vacuum. About 0.5, 1.0, and 1.5 g of membranes were cut into small pieces (0.5 × 0.5 cm²) and dispersed into 100 mL of *tert*-butanol by using a homogenizer (IKA T18, Germany) for up to 10 min at 8000 rotations per minute (rpm) to afford 0.5%, 1.0%, and 1.5% of short nanofibers, respectively.

Preparation of Tubular Scaffolds: To prepare TBS, first, the planar scaffold was obtained by 3D printing of PCL, which involved the nozzle-moving rate of 1.2–1.5 mm s⁻¹, the extrusion rate of 0.01–0.015 mm s⁻¹, the printing temperature of 75 °C, the strand angle of the second layer of 65°, and the strand width of 1.0 mm. Then, the planar scaffolds were curled and mounted on the fixed axis of the required diameter by using a metal-binding wire for fixation. Subsequently, the fixed axis with curled planar scaffold was heated for up to 75 °C for 20 min and then placed at -80 °C for up to 1 h to afford the gap-shaped tubular scaffold. Finally, the PCL strand was printed to fill the gap of the tubular scaffolds (Figure 11b).

Preparation of Tracheal Scaffolds: To prepare tracheal scaffolds, the tubular scaffolds were placed into a mold. Afterward, the uniform dispersion of short nanofibers was poured into the mold, frozen at -80 °C for up to 4 h, and then freeze dried for up to 48 h to achieve tracheal scaffolds. The tracheal scaffolds were crosslinked by glutaraldehyde for up to 6 h to achieve structural stability (Figure 11c).^[46] The tracheal scaffolds impregnated with the SF0.5, SF1.0, and SF1.5 nanofiber aerogels were designated as TSF0.5, TSF1.0, and TSF1.5, respectively. For the in vivo assessment of the biocompatibility, the tracheal scaffolds in the form of a patch were designed, which consisted of an aerogel-planar scaffold-aerogel. Tracheal patches containing 0.5%, 1.0%, and 1.5% of SF were represented as TSF0.5 patch, TSF1.0 patch, and TSF1.5 patch, respectively (Figure 11d). Besides, to evaluate SF aerogels, the equal volume of short nanofiber dispersions was poured into 48-wells cell culture plate, freeze-dried, and crosslinked by glutaraldehyde to afford SF0.5, SF1.0, and SF1.5 aerogels, respectively.

Characterization—Morphological Analysis: Nanofibers and tracheal scaffolds were sputter-coated with gold and their morphology was discerned by SEM (Hitachi TM-1000, Japan) at an accelerating voltage of 5 kV. Short nanofibers were dispersed in ethanol and observed by optical microscope. The length, layer thickness, and diameter of the native trachea (NT), TBS, dry TSF1.0, and wet TSF1.0 ($n = 5$) were measured by a vernier caliper.

Porosity of Scaffolds: The porosity (ρ) of SF0.5, SF1.0, and SF1.5 aerogels was calculated by Equation (1).^[47] The weight of the sample was measured in the dry state and recorded as w_0 . The sample was then transferred to the ethanol for complete immersion and the weight was recorded as w_1 ($n = 5$)

$$\rho = (w_1 - w_0) / (\rho \times v) \quad (1)$$

The porosity of tracheal scaffolds was calculated by Equation (2) as follows

$$\rho = (w_1 - w_0) / [\rho \times (v_2 - v_1)] \quad (2)$$

Where ρ and v represented the density of the ethanol and volume of sample, respectively. The v_1 and v_2 represented the volume of the inner and outer sides of tracheal scaffolds, respectively.

Density of Scaffolds: The density (ρ) of the SF0.5, SF1.0, and SF1.5 aerogels was calculated by Equation (3) ($n = 5$).^[48] by using Equation (3)

$$\rho = m/v = (4m) / (d^2h) \quad (3)$$

The density of the TBS and TSF1.0 was measured by using Equation 4 ($n = 5$)

$$\rho = m/v = (4m) / (d_1 - d_2)^2h \quad (4)$$

Where m and v represented the weight and volume of the sample; d and h indicated the diameter and height of the sample, respectively. The d_1 and d_2 represented the outer and inner diameter of the scaffolds, respectively.

Volume Shrinkage Rate: The volume shrinkage rate (S) of SF0.5, SF1.0, and SF1.5 aerogels was measured by the following method. The volume of the aerogels was recorded as v_0 . Then the SF aerogels were transferred to a vial containing glutaraldehyde vapors for up to 6 h and their volume was recorded as v_1 in the dry state. Afterward, SF aerogels were transferred to deionized water for up to complete immersion and their volume was recorded as v_2 . The volume shrinkage rate of SF aerogels was calculated by Equation (5) ($n = 5$)

$$S = (v_0 - v_x) / v_0 \quad (5)$$

Whereas v_x indicates the volume of the aerogels in the dry (v_1) or wet (v_2) state.

Water Absorption of Scaffolds: The water absorption capacity (w) of SF aerogels and TBS1.0 was calculated by Equation (6).^[49] First, the mass of the sample was measured in the dry state and recorded as w_0 . Afterward, samples were transferred to deionized water for up to complete immersion for up to 1, 3, 5, 10, 20, 50, 90, and 120 min. Wet samples were placed on a paper towel and the excess water was allowed to be drained off. Then the mass of samples in wet state was measured and recorded as w_x . The percentage of the water absorption was calculated by using Equation (6) ($n = 5$)

$$w = (w_x - w_0) / w_0 \times 100\% \quad (6)$$

Mechanical Testing—Longitudinal Tensile Test: The longitudinal tensile test was performed by using a universal testing machine (Instron 3345, USA) with a 200-N load sensor at a strain rate of 5 mm min⁻¹ at room temperature until failure (Figure 4a). The TBS and NT samples were tailored to afford a planar shape, and cut along the longitudinal direction to afford rectangular specimens (30 × 10 mm²). The thickness of the NT and TBS specimens was 0.83 ± 0.02 and 0.79 ± 0.02 mm, respectively. The UTS was calculated from the maximum load before failure and the E was calculated from the linear region of stress-strain curve ($n = 5$).

Radial Compression Test: The radial cyclic loading-unloading fatigue compression tests (for up to 50 cycles) of the TBS, dry TSF1.0, wet TSF1.0, and NT were carried out by using universal testing at a strain rate of 5 mm min⁻¹. The test was stopped as the diameter of the scaffold decreased by 50% of its original diameter ($n = 5$).

Degradation of Scaffolds: The in vitro degradation of TBS, SF1.0 aerogel, and TSF1.0 was assessed in phosphate-buffered saline (PBS, pH = 7.4 ± 0.1). Samples of certain mass (20–60 mg) represented by W_0 were weighed and incubated at 37 °C. At pre-determined time points, the samples were rinsed with the deionized water 3 times, freeze-dried, and weighed again to determine the final weight (W_z). The morphology of dried

samples was observed by optical microscope and SEM. Finally, the remaining mass percentage of the samples was calculated by using Equation (7) ($n = 5$)

$$\text{Remained mass (\%)} = W_z/W_0 \times 100\% \quad (7)$$

Biocompatibility of Scaffolds In Vitro—Hemocompatibility Assessment: Hemolysis test was used to evaluate the blood compatibility of tracheal scaffolds. About 5 mL of fresh blood was obtained from New Zealand rabbits and centrifuged at 3000 rpm for up to 10 min to obtain red blood cells (RBCs). After centrifugation, the RBCs pellets were washed with normal saline three times and then mixed with normal saline (4:5 v/v) to afford RBCs suspension. Each sample (2x2 mm²) was placed in a new tube and 1 mL of RBCs suspension was added at 37 °C for up to 2 h. After incubation, the RBCs suspension was taken from each tube and centrifuged at 3000 rpm for up to 10 min. The supernatant was collected and the optical density (OD) was measured at 540 nm. The normal saline and deionized water served as negative and positive controls, respectively.^[24] The hemocompatibility was calculated by using Equation 8 ($n = 5$)

$$\text{Hemolysis ratio (\%)} = [(A_T - A_N) / (A_P - A_N)] \times 100\% \quad (8)$$

where, A_T represented the OD of the sample. A_P and A_N were the corresponding OD values of positive and negative control groups, respectively.

Cell Seeding Efficiency: Rabbit chondrocytes were cultured in a chondrocyte culture medium (containing 79% of DEME/F12 basic medium, 10% fetal bovine serum (FBS), and 1% penicillin/streptomycin solution). The cell seeding efficiency of the tracheal scaffolds was determined by the following method.^[13] Briefly, chondrocytes suspension (1.0×10^5 cells mL⁻¹) was evenly seeded onto the tracheal scaffold and the cell number was recorded as T_0 . After 4 h of incubation at 37 °C and 5% CO₂, the media from the scaffolds was collected and the cell numbers of media were counted and recorded as T_1 . The cell seeding efficiency of the samples was calculated based on Equation (9) ($n = 3$)

$$\text{Cell seeding efficiency (\%)} = (T_0 - T_1) / T_0 \times 100\% \quad (9)$$

Cytocompatibility: Rabbit chondrocytes (4×10^4 cells per sample) were seeded on scaffold for up to 1, 3, and 7 days, and the medium was changed every other day. Cell-seeded constructs were incubated at 37 °C in a humidified atmosphere containing 5% CO₂. Before cell seeding, the scaffolds were immersed in 75% ethanol for about 6 h for sterilization. At pre-determined time points, cell viability and proliferation were examined by CCK-8 assay and live/dead staining assay, respectively ($n = 3$). For cell proliferation assay, CCK-8 assay kit (Yeasen, Shanghai, China) was used. Samples were washed with PBS for up to three times and incubated with the 200 μL of the assay solution in serum-free medium (DMEM: CCK-8, 9:1 v/v). After incubation for up to 1 h at 37 °C, 100 μL of the suspension was transferred into a 96-well plate to measure the absorbance (450 nm). For live/dead staining of scaffolds at day 3 and 7, the aforementioned scaffolds seeded with chondrocytes were stained with a live-dead cytotoxicity assay kit (MesGen Biotechnology, Shanghai, China) and then observed by confocal laser scanning microscopy (CLSM, Carl Zeiss LSM700, Jena, Germany). The morphology of chondrocytes seeded on scaffolds was analyzed by SEM at day 3 and 7. The cell-seeded scaffolds were subsequently rinsed with PBS and fixed by 4% paraformaldehyde (PFA) and stored at 4 °C for up to 2 h. Finally, the scaffolds were dehydrated with graded ethanol series and sputter-coated with gold for up to 45 s at a current of 5 mA.

Cell Infiltration: Cell infiltration into scaffolds was examined by using H&E staining following a previous method.^[12] For H&E staining, the cell-seeded scaffolds were harvested and fixed in 4% PFA at day 7. Afterward, constructs were dehydrated and embedded into paraffin for sectioning. The cross-sectional specimens were stained with H&E and observed by microscope (TS100, Nikon, Japan).

Performance of Scaffolds In Vivo—Preliminary Evaluation of the Biocompatibility of Scaffolds In Vivo: 1-month-old Balb/c nude mice were obtained from the Shanghai Institute of Materia Medica, Chinese Academy of Sciences, Shanghai, China, and animal experiments were approved by

the Ethics Committee of Shanghai Pulmonary Hospital, Shanghai, China. Mice were anesthetized by an intraperitoneal injection of 0.3 mL of 1% pentobarbital sodium and the skin was excised. Each animal received one TSF1.0 scaffold subcutaneously. Scaffolds were retrieved after 4 weeks, and subjected to H&E staining, Masson's trichrome staining, and CD31 staining. All of the staining results were collected by microscopy (TS100, Nikon, Japan) ($n = 3$).

Evaluation of Cartilage Formation in Vivo: To further elucidate the biocompatibility of scaffolds in vivo, tracheal patches were prepared as described in section titled "Preparation of tracheal scaffolds".^[13] Then the tracheal patches were seeded with chondrocytes (1.0×10^8 cells per sample) and cultured in vitro for up to 1 week, followed by the subcutaneous implantation into nude mice for up to 4 and 8 weeks. At predetermined time points, scaffolds were explanted, fixed in 4% PFA and subjected to sectioning. Explanted scaffolds were stained with H&E, Safranin-O, and collagen type II staining.

Statistical Analysis: All data were collected from at least three independent studies and expressed as mean ± standard error of mean (SEM). Student's *t*-test or one-way analysis of variance (ANOVA) with Tukey's posthoc multiple comparisons were used to analyze significance where appropriate. The criteria for statistical significance were * $p < 0.05$.

Acknowledgements

Zhengchao Yuan and Yijiu Ren are co-first authors. This research was supported by the Fundamental Research Funds for the Central Universities (No. 2232019A3-07), National Nature Science Foundation of China (Nos. 81970091, 32050410286, 31771023, and 3201101259), Science and Technology Commission of Shanghai Municipality (Nos.19441902600, 20S31900900, and 20DZ2254900), Program of Shanghai Academic/Technology Research Leader (No. 19XD1431100), and Sino German Science Foundation Research Exchange Center (No. M-0263). This project was also supported by Researchers Supporting Program of King Saud University, Riyadh, Saudi Arabia (No. RSP-2021/65).

This project was also supported by International Cooperation of 2021-2022 China and Poland Science & Technology Personnel Exchange Program (No. 17) and National Advanced Functional Fiber Innovation Center (2021-fx020301).

Conflict of Interest

The authors declare no conflict of interest.

Data Availability Statement

The data that support the findings of this study are available from the corresponding author upon reasonable request.

Keywords

3D-printing, aerogels, electrospinning, tracheal scaffolds, tissue engineering

Received: August 26, 2021

Revised: October 13, 2021

Published online: November 9, 2021

[1] B. Udelsman, D. J. Mathisen, H. C. Ott, *Ann. Cardiothorac. Surg.* **2018**, *7*, 175.

[2] J. F. de Oliveira, T. P. de Farias, J. M. de Almeida Vital, M. E. G. da Trindade Meira Henriques, M. A. G. da Trindade Meira Henriques, M. E. L. de Moura, in *Tracheostomy 1* (Ed: Y. P. de Farias) Springer-Cham, Berlin **2018**, Ch. 2.

- [3] Z. Wang, F. Sun, Y. Lu, S. Pan, W. Yang, G. Zhang, J. Ma, H. Shi, *Int. J. Artif. Organs* **2021**, *44*, 55.
- [4] D. Li, Z. Yin, Y. Liu, S. Feng, Y. Liu, F. Lu, Y. Xu, P. Min, M. Hou, K. Li, A. He, W. Zhang, W. Liu, Y. Zhang, G. Zhou, Y. Cao, *Acta Biomater.* **2019**, *89*, 206.
- [5] S. L. Bogan, G. Z. Teoh, M. A. Birchall, *J. Cell. Biochem.* **2016**, *117*, 1497.
- [6] C. A. Best, V. K. Pepper, D. Ohst, K. Bodnyk, E. Heuer, E. A. Onwuka, N. King, R. Strouse, J. Grischkan, C. K. Breuer, J. Johnson, T. Chiang, *Int. J. Pediatr. Otorhinolaryngol.* **2018**, *104*, 155.
- [7] C. Crowley, M. Birchall, A. M. Seifalian, *J. Tissue Eng. Regen. Med.* **2015**, *9*, 357.
- [8] Y. D. Tchoukalova, J. M. Hintze, R. E. Hayden, D. G. Lott, *Int. J. Artif. Organs* **2018**, *41*, 100.
- [9] P. Lange, H. Shah, M. Birchall, P. Sibbons, T. Ansari, *J. Biomed. Mater. Res., Part B* **2017**, *105*, 2126.
- [10] M. Shafiq, Y. Jung, S. H. Kim, *J. Biomed. Mater. Res., Part A* **2015**, *103*, 2673.
- [11] A. D. Dikina, D. S. Alt, S. Herberg, A. Mcmillan, H. A. Strobel, Z. Zheng, M. Cao, B. P. Lai, O. Jeon, V. I. Petsinger, C. U. Cotton, M. W. Rolle, E. Alsberg, *Adv. Sci.* **2018**, *5*, 1700402.
- [12] Y. Xu, Z. Wang, Y. Hua, X. Zhu, Y. Wang, L. Duan, L. Zhu, G. Jiang, H. Xia, Y. She, G. Zhou, *Mater. Sci. Eng. C* **2021**, *120*, 111628.
- [13] Y. Xu, L. Duan, Y. Li, Y. She, J. Zhu, G. Zhou, G. Jiang, Y. Yang, *Adv. Funct. Mater.* **2020**, *30*, 1910067.
- [14] H. V. Vu, Q. K. Huynh, V. D. Q. Nguyen, *J. Cardiothorac. Surg.* **2019**, *14*, 49.
- [15] S. Dharmadhikari, L. Liu, K. Shontz, M. Wiet, A. White, A. Goins, H. Akula, J. Johnson, S. D. Reynolds, C. K. Breuer, T. Chiang, *Acta Biomater.* **2020**, *102*, 181.
- [16] C.-Y. Liaw, S. Ji, M. Guvendiren, *Adv. Healthcare Mater.* **2018**, *7*, 1701165.
- [17] S. Xu, Q. Li, H. Pan, Q. Dai, Q. i Feng, C. Yu, X. Zhang, Z. Liang, H. Dong, X. Cao, *ACS Biomater. Sci. Eng.* **2020**, *6*, 6896.
- [18] Y. She, Z. Fan, L. Wang, Y. Li, W. Sun, H. Tang, L. Zhang, L. Wu, H. Zheng, C. Chen, *Front. Cell Dev. Biol.* **2021**, *9*, 629796.
- [19] S. Pan, Y. Zhong, Y. Shan, X. Liu, Y. Xiao, H. Shi, *J. Biomed. Mater. Res., Part A* **2019**, *107*, 360.
- [20] Y. Chen, Z. Jia, M. Shafiq, X. Xie, X. Xiao, R. Castro, J. Rodrigues, J. Wu, G. Zhou, X. Mo, *Colloids Surf., B* **2021**, *201*, 111637.
- [21] B. Sun, Z. Zhou, T. Wu, W. Chen, D. Li, H. Zheng, H. El-Hamshary, S. S. Al-Deyab, X. Mo, Y. Yu, *ACS Appl. Mater. Interfaces* **2017**, *9*, 26684.
- [22] Y. Li, Q. Li, H. Li, X. Xu, X. Fu, J. Pan, H. Wang, J. Y. H. Fuh, Y. Bai, S. Wei, *J. Biomed. Mater. Res., Part B* **2020**, *51*, 16647.
- [23] W. Chen, J. Ma, L. Zhu, Y. Morsi, H. El-Hamshary, S. S. Al-Deyab, X. Mo, *Colloids Surf., B* **2016**, *142*, 165.
- [24] R. Kandi, P. M. Pandey, M. Majood, S. Mohanty, *Rapid Prototyp. J.* **2021**, *27*, 421.
- [25] I. G. Kim, S. A. Park, S. H. Lee, J. S. Choi, H. Cho, S. J. Lee, Y. W. Kwon, S. K. Kwon, *Sci. Rep.* **2020**, *10*, 4326.
- [26] W. Chen, Y. Xu, Y. Li, L. Jia, X. Mo, G. Jiang, G. Zhou, *Chem. Eng. J.* **2020**, *382*, 122986.
- [27] K. Zhang, N. Cao, X. Guo, Q. Zou, S. Zhou, R. Yang, W. Zhao, X. Mo, W. Liu, Q. Fu, *NeuroUrol. Urodyn.* **2018**, *37*, 978.
- [28] Q. Yao, J. G. L. Cosme, T. Xu, J. M. Miszuk, P. H. S. Picciani, H. Fong, H. Sun, *Biomaterials* **2017**, *115*, 115.
- [29] R. Machino, K. Matsumoto, D. Taniguchi, T. Tsuchiya, Y. Takeoka, Y. Taura, M. Moriyama, T. Tetsuo, S. Oyama, K. Takagi, T. Miyazaki, G. Hatachi, R. Doi, K. Shimoyama, N. Matsuo, N. Yamasaki, K. Nakayama, T. Nagayasu, *Adv. Healthcare Mater.* **2019**, *8*, 1800983.
- [30] L. Yijing, Y. Su, Y. Lin, L. He, L. Wu, X. Hou, C. Zheng, *Build. Environ.* **2020**, *184*, 107229.
- [31] Y. Xu, Y. Li, Y. Liu, H. Li, Z. Jia, Y. Tang, G. Jiang, X. Zhang, L. Duan, *Am. J. Transl. Res.* **2019**, *11*, 5390.
- [32] N. Zhong, T. Dong, Z. Chen, Y. Guo, Z. Shao, X. Zhao, *J. Biomater. Appl.* **2019**, *34*, 3.
- [33] S. J. Lee, J. S. Choi, M. R. Eom, H. H. Jo, I. K. Kwon, S. K. Kwon, S. A. Park, *Nanoscale* **2020**, *12*, 4846.
- [34] H.-C. Han, J. K. W. Chesnutt, J. R. Garcia, Q. Liu, Q. Wen, *Ann. Biomed. Eng.* **2013**, *41*, 1399.
- [35] M. Shafiq, L. Wang, D. Zhi, Q. Zhang, K. Wang, L. Wang, D. -H. Kim, D. Kong, S. H. Kim, *J. Biomed. Mater. Res., Part B* **2019**, *107*, 1669.
- [36] G. Poologasundarampillai, D. Wang, S. Li, J. Nakamura, R. Bradley, P. D. Lee, M. M. Stevens, D. S. Mcphail, T. Kasuga, J. R. Jones, *Acta Biomater.* **2014**, *10*, 3733.
- [37] C. Deng, R. Lin, M. Zhang, C. Qin, Q. Yao, L. Wang, J. Chang, C. Wu, *Adv. Funct. Mater.* **2019**, *29*, 1806068.
- [38] L. L. Y. Chiu, M. Montgomery, Y. Liang, H. Liu, M. Radisic, *Proc. Natl. Acad. Sci. USA* **2012**, *11*, 109.
- [39] Y. Arima, H. Iwata, *Biomaterials* **2007**, *28*, 3074.
- [40] C. R. Butler, R. E. Hynds, C. Crowley, K. H. C. Gowers, L. Partington, N. J. Hamilton, C. Carvalho, M. Platé, E. R. Samuel, A. J. Burns, L. Urbani, M. A. Birchall, M. W. Lowdell, P. De Coppi, S. M. Janes, *Biomaterials* **2017**, *124*, 95.
- [41] Y. Chen, W. Xu, M. Shafiq, J. Tang, J. Hao, X. Xie, Z. Yuan, X. Xiao, Y. Liu, X. Mo, *J. Colloid Interface Sci.* **2021**, *603*, 94.
- [42] S. Patel, K. Kurpinski, R. Quigley, H. Gao, B. S. Hsiao, M.-M. Poo, S. Li, *Nano Lett.* **2007**, *7*, 2122.
- [43] W. Chen, Y. Xu, Y. Liu, Z. Wang, Y. Li, G. Jiang, X. Mo, G. Zhou, *Mater. Des.* **2019**, *179*, 107886.
- [44] H. Jing, B. Gao, M. Gao, H. Yin, X. Mo, X. Zhang, *Artif. Cells, Nanomed. Biotechnol.* **2018**, *46*, 985.
- [45] J. Chen, D. Sheng, T. Ying, H. Zhao, J. Zhang, Y. Li, H. Xu, S. Chen, *Nano-Micro Lett.* **2021**, *13*, 23.
- [46] W. Chen, S. Chen, Y. Morsi, H. El-Hamshary, M. El-Newhy, C. Fan, X. Mo, *ACS Appl. Mater. Interfaces* **2016**, *8*, 24415.
- [47] D. J. Huey, J. C. Hu, K. A. Athanasiou, *Science* **2012**, *338*, 917.
- [48] G. Duan, S. Jiang, V. Jérôme, J. H. Wendorff, A. Fathi, J. Uhm, V. Altstadt, M. Herling, J. Breu, R. Freitag, S. Agarwal, A. Greiner, *Adv. Funct. Mater.* **2015**, *25*, 2850.
- [49] S. K. Ramadass, S. Perumal, A. Gopinath, A. Nisal, S. Subramanian, B. Madhan, *ACS Appl. Mater. Interfaces* **2014**, *6*, 15015.
- [50] D. Xia, D. Jin, Q. Wang, M. Gao, J. Zhang, H. Zhang, J. Bai, B. Feng, M. Chen, Y. Huang, Y. Zhong, N. Witman, W. Wang, Z. Xu, H. Zhang, W. Fu, M. Yin, *SSRN Electron. J.* **2020**, <https://doi.org/10.2139/ssrn.3280654>.
- [51] M. Shafiq, S. H. Kim, *Macromol. Res.* **2016**, *24*, 986.
- [52] M. Mader, V. Jérôme, R. Freitag, S. Agarwal, A. Greiner, *Biomacromolecules* **2018**, *19*, 1663.
- [53] D. Xia, D. Jin, Q. Wang, M. Gao, J. Zhang, H. Zhang, J. Bai, B. Feng, M. Chen, Y. Huang, Y. Zhong, N. Witman, W. Wang, Z. Xu, H. Zhang, M. Yin, W. Fu, *J. Tissue Eng. Regen. Med.* **2019**, *13*, 694.
- [54] D. Ke, H. Yi, S. Est-Witte, S. George, C. Kengla, S. J. Lee, A. Atala, S. V. Murphy, *Biofabrication* **2020**, *12*, 1.
- [55] K. A. Van Kampen, E. Olaret, I.-C. Stancu, L. Moroni, C. Mota, *Mater. Sci. Eng. C* **2021**, *119*, 111472.
- [56] F. J. Chaparro, M. E. Matusicky, M. J. Allen, J. J. Lannutti, *J. Biomed. Mater. Res., Part B* **2016**, *104*, 1525.
- [57] L. A. Bosworth, S. Downes, *Polym. Degrad. Stab.* **2010**, *95*, 2269.
- [58] D. Vernon, D. F. Eytan, A. Hillel, K. Boahene, *Laryngoscope* **2021**.
- [59] F. Yongcong, T. Zhang, L. Liverani, A. R. Boccaccini, W. Sun, *J. Biomed. Mater. Res., Part A* **2019**, *107*, 2694.